Available online at www.sciencedirect.com
ScienceDirect
International Journal of Multiphase Flow 34 (2008) 484–501
International Journal of Multiphase Flow
www.elsevier.com/locate/ijmulflow

An Eulerian–Eulerian model for gravity currents driven by inertial particles

Mariano I. Cantero [a,b,*], S. Balachandar [b], Marcelo H. García [a]

[a] Departments of Civil and Environmental Engineering and Geology, University of Illinois at Urbana-Champaign, 205 N. Mathews Avenue, HSL #2525, Urbana, IL 61801, USA

[b] Department of Mechanical and Aerospace Engineering, University of Florida, Gainesville, FL 32611, USA

Received 23 March 2007; received in revised form 16 August 2007

Abstract

In this work we introduce an Eulerian–Eulerian formulation for gravity currents driven by inertial particles. The model is based on the equilibrium Eulerian approach and on an asymptotic expansion of the two-phase flow equations. The final model consists of conservation equations for the continuum phase (carrier fluid), an algebraic equation for the disperse phase (particles) velocity that accounts for settling and inertial effects, and a transport equation for the disperse phase volume fraction. We present highly resolved two-dimensional (2D) simulations of the flow for a Reynolds number of $Re = 3450$ (this particular choice corresponds to a value of Grashof number of $Gr = Re^2/8 = 1.5 \times 10^6$) in order to address the effect of particle inertia on flow features. The simulations capture physical aspects of two-phase flows, such as particle preferential concentration and particle migration down turbulence gradients (turbophoresis), which modify substantially the structure and dynamics of the flow. We observe the migration of particles from the core of Kelvin–Helmholtz vortices shed from the front of the current as well as their accumulation in the current head. This redistribution of particles in the current affects the propagation speed of the front, bottom shear stress distribution, deposition rate and sedimentation. This knowledge is helpful for the interpretation of the geologic record.

Keywords: Turbidity currents; Gravity currents; Density currents; Sediment deposits; Bottom shear stress; Two-phase flow; Equilibrium Eulerian model; Spectral methods

1. Introduction

Gravity or density currents are flows driven by lateral pressure gradients produced by the action of gravity on fluids with different density. The density difference can be due to scalar fields such as temperature or salinity for which the excess density is conserved over the bulk, or by particles in suspension that may settle or be re-entrained into the flow. For this reason particle-driven gravity currents are also known as non-conservative gravity currents (García, 1992).

Particulate gravity currents, commonly known as turbidity currents, can be observed in many engineering, environmental and geological applications and they are the focus of the present work. In most of the cases the currents are dilute and the density difference is only a few percents, however, this is enough to trigger swift flows with a large transport capacity of mass and energy. Bagnold (1962) was among the first to discuss the conditions for auto-suspending turbidity currents. The sediment deposits generated by turbidity currents have also been of great interest to petroleum geologists (Kuenen and Migliorini, 1950). One of the most interesting property of particulate gravity currents is that they can modify their driving force via deposition and resuspension of particles. If particle entrainment prevails over deposition, the current will eventually accelerate and attain very high velocities (Parker

* Corresponding author. Address: Departments of Civil and Environmental Engineering and Geology, University of Illinois at Urbana-Champaign, 205 N. Mathews Avenue, HSL #2525, Urbana, IL 61801, USA. Tel.: +1 217 333 6904; fax: +1 217 333 0687.
E-mail address: mcantero@uiuc.edu (M.I. Cantero).

0301-9322/$ - see front matter © 2007 Elsevier Ltd. All rights reserved.
doi:10.1016/j.ijmultiphaseflow.2007.09.006

et al., 1986). In the ocean, for example, sediment slumps can trigger gravity currents capable of traveling very long distances (Heezen and Ewing, 1952; Mohrig et al., 1998). These strong flows can carve out submarine canyons (Fukushima et al., 1985) and mold the seabed producing different bedforms patterns such as ripples, dunes, antidunes and gullies (Allen, 1985). The dynamics of particulate gravity currents is also relevant for dusty thunderstorm fronts (Droegemeier and Wilhelmson, 1987), pyroclastic flows produced in volcano eruptions (Sparks et al., 1991), aerosol releases in the environment, flows originated by the discharge of a sediment-laden flow into a lake (Normark and Dickson, 1976) and snow avalanches (Hopfinger, 1983). Many more examples can be found in the books by Simpson (1997) and Allen (1985).

Particulate gravity currents have received a vast amount of attention in the past. García and Parker (1989) investigated the formation of internal hydraulic jumps produced when a current finds a change in slope. The formation of the jump is associated with a change in the flow regime and influences sediment transport capacity. García et al. (1993) studied the erosion capacity of gravity currents and developed an empirical entrainment function that links the bottom shear stress with the rate of sediment entrainment into suspension. Depositional particulate gravity currents have been studied by Gladstone et al. (1998) for bidisperse particles and by Altinakar et al. (1990) and García (1994) in the context of poorly sorted sediment. Bonnecaze et al. (1993), Bonnecaze et al. (1995), Bonnecaze and Lister (1999) and de Rooij and Dalziel (2001) have studied depositional gravity currents in planar and cylindrical geometrical settings. Best et al. (2001) have focused on mean flow and turbulence structure of particulate gravity currents. Shallow water equation models have been used to study the dynamics of particulate currents and resulting deposition patterns (Bonnecaze et al., 1993; Choi and García, 1995). Recently, fully resolved simulations (Necker et al., 2002; Necker et al., 2005; Blanchette et al., 2005) have been performed for particle-driven gravity currents. These simulations have allowed clear interpretation of the flow dynamics and their relation to depositional patterns.

Particulate currents differ from thermal or saline currents in their fundamental feature that the particles, which are the source of density variation, do not exactly follow the fluid. In contrast, in the case of scalar currents the thermal or saline concentration fields are advected at the local fluid velocity. In the limit of small particles the primary source of relative velocity between the particles and the surrounding fluid is due to gravity induced settling of particles. Most prior theoretical and numerical investigations of particulate currents have been limited to this regime. The velocity of particles in these studies is chosen to differ from the local fluid velocity by a constant settling velocity in the direction of gravity and the settling velocity is typically assumed to be the same as that of an isolated particle freely settling in still fluid.

Several geological phenomena involve the transport of coarse particles by gravity currents. Such finite sized particles do not follow the surrounding fluid exactly and settling velocity is only one of the mechanisms contributing to the relative velocity. The finite inertia of the particles becomes important with additional contribution to relative velocity arising from the inertial response of particles in regions of strong fluid acceleration. In regions of rectilinear fluid acceleration (or deceleration), inertial particles may lag (or lead) the fluid substantially. Also, in regions of curved streamlines the particle pathlines may not curve as rapidly as the fluid surrounding them. In the context of high Reynolds number turbulent flows it is well known that inertial particles tend to exhibit preferential concentration, with local accumulation in regions of high strain-rate and avoiding regions of high vorticity (Squires and Eaton, 1991; Wang and Maxey, 1993). In the context of gravity currents, this has implications for the distribution of particles in the highly vortical regions of the front of the current and along the interface between the heavy and the light fluids. Since the density difference due to the suspended particles is the main cause of the flow, the redistribution of particles will in turn alter the dynamics of the current. Furthermore, processes such as deposition, erosion and resuspension can also be influenced by the inertial behavior of the particles.

In this work we focus attention on the effect of particle inertia on the dynamics of the particulate gravity current. We will also address the influence on flow features and deposition patterns. We use the equilibrium Eulerian approach (Ferry and Balachandar, 2001; Ferry et al., 2002; Ferry et al., 2003) to account for the inertial effect of particles. The advantage of this approach is that the relative velocity between the particles and the surrounding fluid flow is given by an explicit expression, without having to solve additional equations for the particulate velocity field. The equilibrium Eulerian velocity and the mathematical model to be employed is presented in Section 2, which is followed by a brief description of the formulation of the problem in Section 3. In Section 4 the numerical methodology is described. Then, we present two-dimensional (2D) direct numerical simulations and assess the effect of finite inertia on the current structure, front velocity, bed shear stress and deposition pattern in Section 5. Finally, summary and conclusions are drawn in Section 6.

2. Mathematical model

We are interested in simulating buoyant flows driven by the presence of solid particles of finite size. In this situation particles not only modify the bulk density as in the dusty gas formulation (Marble, 1970), but move at a velocity that differs from the local surrounding fluid velocity. We limit attention to dilute suspensions where the volume concentration of particles (ϕ_d) is taken to be small. Particle concentration will be considered to be low not only in the mean, but also locally even in regions of preferential accumulation, and thus complex issues surrounding local inter-

particle interactions will be ignored. The effective density variation within the flow will be sufficiently low that we will employ Boussinesq approximation. The inertial effect of the particles is the focus of this study and thus the relative velocity between the particles and the surrounding flow is due to both gravitational settling and particle inertia. However, dimensionless particle inertia, defined in terms of Stokes number ($\tilde{\tau}$-ratio of particle time scale to fluid time scale), will be considered sufficiently small that equilibrium approximation can be used (Ferry and Balachandar, 2001; Ferry et al., 2002; Ferry et al., 2003). By limiting $\tilde{\tau}$ to sufficiently small values we can express the particle velocity in terms of surrounding fluid velocity. For the case of large $\tilde{\tau}$, a Lagrangian treatment of particles is required since the effect of initial conditions does not decay sufficiently rapidly. Here we develop a new formulation that includes the role of particle inertia in the interest to simulate gravity currents at environmental and geological scales. In this section we present an Eulerian–Eulerian model based on an asymptotic expansion of the two-phase flows equations in parameters describing the (dimensionless) particle inertia ($\tilde{\tau}$) and the (dimensionless) particle volumetric concentration ($\tilde{\phi}_d$). The model is formally exact to $O(\tilde{\tau}\tilde{\phi}_d + \tilde{\tau}^2 + \tilde{\phi}_d^2)$ and consists of conservation equations for the continuous phase (carrier fluid), an algebraic equation for the disperse phase (particles) velocity, and a transport equation for the particle volume fraction.

Let indices c and d denote the continuous and disperse phases, respectively. We denote the densities, volume fractions, and velocities of each phase by ρ_c, ϕ_c, $\mathbf{u}_c$, and ρ_d, ϕ_d, $\mathbf{u}_d$, respectively. In the case of constant density phases and no mass transfer between phases the mass conservation equations can be expressed as (Zhang and Prosperetti, 1997; Drew and Passman, 1998)

$$\frac{\partial \phi_c}{\partial t} + \nabla(\phi_c \mathbf{u}_c) = 0 \qquad \text{and} \tag{1}$$

$$\frac{\partial \phi_d}{\partial t} + \nabla(\phi_d \mathbf{u}_d) = 0, \tag{2}$$

where $\phi_c + \phi_d = 1$.

The process of obtaining the ensemble-averaged momentum equations and their closure have been discussed in detail in the literature (Joseph and Lundgren, 1990; Zhang and Prosperetti, 1997; Drew and Passman, 1998; Machioro et al., 1999; Prosperetti, 2001). The resulting momentum equations for the continuous and disperse phases can be expressed as

$$\phi_c \rho_c \frac{D_c \mathbf{u}_c}{Dt} = -\phi_c \nabla p + \mu_c \nabla^2 \mathbf{u}_v - \mathbf{F}, \tag{3}$$

$$\phi_d \rho_d \frac{D_d \mathbf{u}_d}{Dt} = \phi_d(\rho_d - \rho_c)\mathbf{g} - \phi_d \nabla p + \mathbf{F}. \tag{4}$$

Here D_c/Dt and D_d/Dt indicate material derivatives following the continuous phase velocity and the disperse phase velocity, respectively, p is the dynamic pressure in the continuous phase (i.e. the potential $\rho_c \mathbf{x}\cdot\mathbf{g}$ has been subtracted), μ_c is the dynamic viscosity of the continuous phase, $\mathbf{g}$ is the gravity vector, and $\mathbf{F}$ is the net hydrodynamic interaction between phases. Observe that the viscous term is a function of the volume averaged velocity $\mathbf{u}_v = \phi_c \mathbf{u}_c + \phi_d \mathbf{u}_d$ (see Machioro et al., 1999).

For small particles, whose time scale is sufficiently smaller than the flow time scale defined in terms of the maximal compressional strain-rate, an Eulerian field representation for particle velocity can be used and the equation of motion for the particles can be solved explicitly to obtain an explicit expansion for the particle velocity field as (Ferry and Balachandar, 2001)

$$\mathbf{u}_d \approx \mathbf{u}_c + \mathbf{V}_s - \tau(1-\beta)\frac{D_c \mathbf{u}_c}{Dt}, \tag{5}$$

where τ is the particle response time, β depends on the particle to fluid density ratio ($\rho = \rho_d/\rho_c$), and $\mathbf{V}_s$ is the still fluid settling velocity of the particle, which are given by

$$\tau = \frac{d^2(\rho + 1/2)}{18 \nu_c f}, \qquad \beta = \frac{3}{2\rho + 1}, \qquad \text{and}$$
$$\mathbf{V}_s = \tau(1-\beta)\mathbf{g}. \tag{6}$$

Here d is the particle diameter, $f = 1 + 0.15 Re_P^{0.687}$ is the correction for non-Stokesian drag (Crowe et al., 1998) that depends on particle Reynolds number $Re_P = d|\mathbf{u}_c - \mathbf{u}_d|/\nu_c$, and ν_c is the kinematic viscosity of the continuous phase. The particles have been assumed to be spherical and as a result the added mass coefficient is taken to be 1/2. In Eq. (5) it is assumed that the ratio of settling velocity to the ambient flow velocity is small and of the order of Stokes number. It can be shown that implicit in the equilibrium approximation for particle velocity given in Eq. (5) is the assumption

$$\frac{D_d \mathbf{u}_d}{Dt} \approx \frac{D_c \mathbf{u}_c}{Dt}. \tag{7}$$

Eq. (7) can be used to eliminate $D_d \mathbf{u}_d/Dt$ from Eq. (4), which can be combined with Eq. (3) to obtain

$$[\rho_c + \phi_d(\rho_d - \rho_c)]\frac{D_c \mathbf{u}_c}{Dt} = \phi_d(\rho_d - \rho_c)\mathbf{g} - \nabla p + \mu_c \nabla^2 \mathbf{u}_v. \tag{8}$$

We consider the setting depicted in Fig. 1, where a channel is filled at one end with the particulate mixture and is separated by a gate from the rest of the channel, which is filled with clear fluid. When the simulation begins the gate is lifted and the flow develops forming an underflow intrusion of the mixture into the clear fluid (denoted by a solid line in Fig. 1). Let the height of the channel (H) be the length scale, $U = \sqrt{g\Phi(\rho - 1)H}$ be the velocity scale and the initial volume fraction (Φ) be the particle volumetric concentration scale, where g is the magnitude of the gravitational acceleration. The time and pressure scales are correspondingly defined as H/U and $\rho_c U^2$, respectively. We consider density variations to be small and use Boussinesq approximation. The resulting governing equations in the dimensionless form are

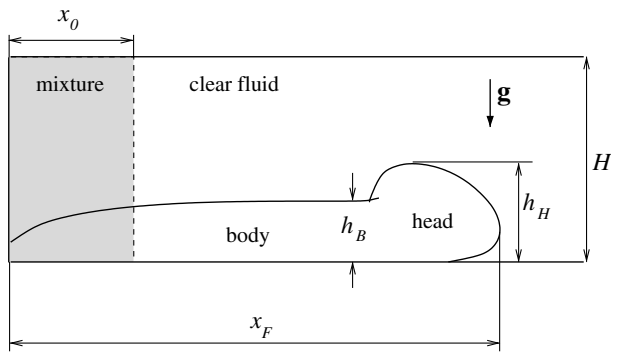

Fig. 1. Sketch of a gravity current and nomenclature used in this work. The flow is started from the initial condition shown by the shaded region between dash lines. As the flow evolves, the intruding front develops the structure of a head followed by a body.

$$\frac{D_c\tilde{\mathbf{u}}_c}{D\tilde{t}} = \tilde{\phi}_d\,\mathbf{e}^g - \nabla\tilde{p} + \frac{1}{Re}\nabla^2\tilde{\mathbf{u}}_v, \tag{9}$$

$$\nabla\tilde{u}_v = 0, \tag{10}$$

$$\tilde{\mathbf{u}}_d = \tilde{\mathbf{u}}_c + \widetilde{\mathbf{V}}_s - \tilde{\tau}\frac{D_c\tilde{\mathbf{u}}_c}{D\tilde{t}}, \quad \text{and} \tag{11}$$

$$\frac{\partial\tilde{\phi}_d}{\partial\tilde{t}} + \nabla(\tilde{\phi}_d\tilde{\mathbf{u}}_d) = \frac{1}{Sc\,Re}\nabla^2\tilde{\phi}_d. \tag{12}$$

Here all dimensionless terms are denoted by a tilde on top, and $\mathbf{e}^g$ is a unit vector pointing in the direction of gravity.

The Reynolds number, defined as $Re = UH/\nu_c$ characterizes the strength of the current. $Sc = \nu_c/\kappa$ is the Schmidt number, where κ is the diffusivity of particles. The other two controlling parameters define the suspended particles in terms of particle Stokes number, $\tilde{\tau}$, and dimensionless settling velocity, $\widetilde{\mathbf{V}}_s$, defined as

$$\tilde{\tau} = \frac{\tau(1-\beta)U}{H} \quad \text{and} \quad \widetilde{\mathbf{V}}_s = \frac{\mathbf{V}_s}{U}, \tag{13}$$

respectively. These parameters characterize the inertial and settling effects of the particle, respectively.

Note that for numerical stability of the spectral method it is common practice to add a diffusion term to Eq. (12). In the limit of $\tilde{\tau} \to 0$ and $|\widetilde{\mathbf{V}}_s| \to 0$ the above governing equations reduce to those corresponding to a scalar gravity current for which this term accounts for the diffusion of the scalar field. In the present case of a particulate gravity current this term can be taken to account for the departure of particle motion from equilibrium prediction. Such departures arise from close interaction of particles, and in general, diffusivity is a function of both local particle concentration and local shear (Acrivos, 1995; Foss and Brady, 2000). Nevertheless, solution of Eq. (12) with little or no diffusion is numerically unstable, especially in the context of spectral simulations.

According to Eq. (11) for $\tilde{\tau} = 0$ the particle velocity is simply the sum of local fluid velocity and the still fluid settling velocity. This is the limit often considered in the case of particulate currents. The last term on Eq. (11) arises from the inertial behavior of particles and it accounts for the velocity difference due to the inability of finite inertia particles to move with the fluid in regions of fluid acceleration. It must be pointed out that this term is only the first order correction of $O(\tilde{\tau})$ and, as shown in Ferry and Balachandar (2001), higher order terms of the expansion can be formally derived starting from the equation of motion for the particles. Numerical tests in a variety of turbulent flows have shown that the $O(\tilde{\tau})$ correction included in Eq. (11) is adequate to capture important inertial behaviors such as preferential accumulation and turbophoretic migration of particles of $\tilde{\tau} \leqslant 0.3$ (Ferry and Balachandar, 2001; Ferry et al., 2002; Ferry et al., 2003; Shotorban and Balachandar, 2006).

Note that from Eq. (11) we can express the volume averaged mixture velocity as $\mathbf{u}_v = \mathbf{u}_c + \phi_d\,\mathbf{V}_s + O(\tilde{\tau}\,\tilde{\phi}_d)$. From which it follows that to $O(\tilde{\tau}\,\tilde{\phi}_d)$ we can approximate

$$\nabla^2\tilde{\mathbf{u}}_v \approx \nabla^2\tilde{\mathbf{u}}_c \quad \text{and} \quad \nabla\cdot\tilde{\mathbf{u}}_c \approx 0. \tag{14}$$

The set of governing Eq. (9)–(12), with the approximations in Eq. (14) form a complete Eulerian–Eulerian system of equations for two-phase flows that include particle settling and inertia effects. The equations are formally accurate to $O\left(\tilde{\tau}\tilde{\phi}_d + \tilde{\tau}^2 + \tilde{\phi}_d^2\right)$. The main advantage of this system compared to the original set of equations, i.e. Eq. (1)–(4), is that the momentum equation for the dispersed phase need not be solved as the particle velocity field is expressed algebraically in terms of local fluid velocity by Eq. (11). Another advantage is that the mathematical structure of the simplified governing equations is similar to the standard single fluid incompressible Navier–Stokes equations, and this allows the use of standard techniques developed for incompressible flows for the present problem.

3. Formulation of the problem

Here we will examine the importance of particle inertia and settling under typical scenarios encountered in industrial, geological and environmental applications. From the definition of the length, velocity and time scales introduced above, the particle Stokes number and dimensionless settling velocity can be written as

$$\tilde{\tau} = \left[\frac{(\rho-1)^{5/3}g^{2/3}}{18 f \nu_c^{4/3}}\right] d^2\Phi^{2/3}Re^{-1/3} \quad \text{and} \tag{15}$$

$$\widetilde{V}_s = \frac{\tilde{\tau}}{(\rho-1)\Phi}. \tag{16}$$

Consider the case of a turbidity current with sand particles suspended in water. If we consider sand to water density ratio to be about $\rho \approx 2.65$, and if we assume the relative motion of particles with respect to the surrounding fluid to be in the Stokes regime ($f = 1$), then the prefactor within the square parenthesis in the above equation can be estimated to be $5.9 \times 10^7\ \mathrm{m}^{-2}$. Now if we consider a suspension of 250 μm sand particles at a volume concentration of $\Phi = 1\%$ in a modest gravity current of $Re = 10000$, the resulting Stokes number based on mean flow time scale

is 0.0079. The Stokes number will increase for larger particles and at higher concentration, but will decrease slowly with increasing intensity of the current (i.e. increasing Re).

If we consider the example of dust storms, where sand particles are suspended in air ($\rho \approx 2000$), the prefactor in Eq. (15) becomes 2.4×10^{11} m^{-2}. Now consider a suspension of 50 μm particles at a volume concentration of $\Phi = 0.1\%$ in a current of $Re = 10000$. The corresponding Stokes number becomes $\tilde{\tau} = 0.28$.

From (16) it can be readily seen that in a dilute suspension ($\Phi \sim O(10^{-2})$) of light particles ($\rho \sim O(1)$), as in the case of turbidity currents, the relative magnitude of the settling velocity can be much larger than the Stokes number. On the other hand, for the case of heavy particles ($\rho \sim O(10^3)$) Stokes number can be much larger than dimensionless settling velocity at sufficiently large concentration.

It is reasonable to nondimensionalize the settling velocity of particles with the velocity scale of the current, to gauge the relative importance of particle settling. In contrast, the Stokes number as defined above in Eq. (13) accurately captures only the inertial response of particles to mean scale motion. It is of interest to explore how particle inertia and settling velocity scale with the smaller scales of the flow. Crude estimates of the Kolmogorov velocity and time scales (u_k and τ_k) can be expressed in terms of the Reynolds number of the flow as (see for example Pope, 2000)

$$\frac{T}{\tau_k} \sim Re^{1/2} \quad \text{and} \quad \frac{U}{u_k} \sim Re^{1/4}, \tag{17}$$

from which it follows that

$$\tau^+ = \tilde{\tau}\frac{T}{\tau_k} \sim Re^{1/6} \quad \text{and} \quad V_s^+ = \widetilde{V}_s \frac{U}{u_k} \sim Re^{-1/12}. \tag{18}$$

The inertial response of particles to turbulent eddies is at its maximum when the time scale of the eddies matches that of the particles. Eddies which are larger are of longer time scale and they simply advect the particles, while eddies much smaller are of shorter time scale and do not last long enough to affect the particle motion. As illustrated in (17), with increasing Re a wide range of time scales can be expected within the flow. Thus, we see that even though $\tilde{\tau}$, which is based on mean flow scaling, may be much weaker for inertial response of particles, at high enough Reynolds number, some of the smaller scales of motion will be of appropriate time scale for inertial response of the particles. As we will see below in the simulations to be presented, even modest values of $\tilde{\tau} \sim 0.025$ result in significant inertial response from the particles.

In this work, we present 2D direct numerical simulations for $Re = 3450$. This particular choice corresponds to the same value of Grashof number of $Gr = g\Phi(\rho - 1)H^3/\nu_c^2 = 1.5 \times 10^6$ used by Necker et al. (2002). We address the effect of particle inertia on the flow structure, dynamics, bed shear stress and deposition patterns by varying the parameter $\tilde{\tau}$. In order to isolate the physics of particle inertia, the present investigation neglects any interaction with the bottom. We consider a pure depositional flow without any resuspension and thus avoid the use of empirical particle resuspension relations (García et al., 1993).

4. Numerical approach

The dimensionless governing equations are solved using a de-aliased pseudospectral code (Canuto et al., 1988). Fourier expansions are employed for the flow variables in the horizontal direction (x). In the inhomogeneous vertical direction (z) a Chebyshev expansion is used with Gauss–Lobatto quadrature points. An operator splitting method is used to solve the momentum equation along with the incompressibility condition. With this method the flow field is advanced from time $\tilde{t}^{(n)}$ to $\tilde{t}^{(n+1)}$ in two steps. First, an advection–diffusion equation is used to advance from time level $\tilde{t}^{(n)}$ to an intermediate time level. After the intermediate level velocity field is determined, a Poisson equation is solved to compute the pressure field. Finally, a pressure correction step is used to advance the flow velocities to the level $\tilde{t}^{(n+1)}$ (see for example Brown et al., 2001). A low-storage mixed third order Runge-Kutta and Crank-Nicolson scheme is used for the temporal discretization of the advection–diffusion terms. This scheme is carried out in three stages. The time step from level $\tilde{t}^{(n)}$ to level $\tilde{t}^{(n+1)}$, $\Delta\tilde{t}$, is split into three smaller steps, with pressure correction at the end of each step. More details on the implementation of this numerical scheme can be found in Cortese and Balachandar (1995).

The computational domain is a box of size $\widetilde{L}_x = 25 \times \widetilde{L}_z = 1$, which extends from $\tilde{x} = -12.5$ to $\tilde{x} = 12.5$ and from $\tilde{z} = 0$ to $\tilde{z} = 1$. The flow is initialized from rest with $\tilde{\phi}_d = 1$ in $\tilde{x} \in (-1, 1)$ for all $\tilde{z}$, and $\tilde{\phi}_d = 0$ otherwise with a smooth transition. The details of the initial condition can be found in Cantero et al. (2006). This setting of the problem generates two currents moving from the center outward. The solution was advanced in time until the front reached location of $\tilde{x} = \pm 11.5$ to avoid the influence of finite domain size (Härtel et al., 2000; Cantero et al., 2007b). The simulations were performed using a resolution of $N_x = 1536 \times N_z = 150$. It must be mentioned that more resolution is needed for the particulate flow simulations compared to the corresponding scalar case (i.e. same Re with $\tilde{\tau} = 0$ and $\widetilde{\mathbf{V}}_s = 0$).

Periodic boundary conditions are enforced for all the variable in the horizontal direction. This is done due to the characteristics of the spectral method used, however, the computational domain is taken to be long enough in the streamwise direction to allow free unhindered development of the current for a long time. At the top and bottom walls no-slip and no-penetration conditions are enforced for the continuous phase velocity. For the normalized concentration of particles we apply

$$\widetilde{V}_{sz}\tilde{\phi}_d - \frac{1}{ScRe}\frac{\partial\tilde{\phi}_d}{\partial\tilde{z}} = 0, \quad \text{and} \quad \frac{\partial\tilde{\phi}_d}{\partial\tilde{z}} = 0, \tag{19}$$

respectively, for the top and bottom walls, where $\widetilde{V}_{sz}$ is the wall normal component of the normalized particle

settling velocity. Volume integration of the normalized concentration Eq. (12) on the computational domain V shows that

$$\frac{\mathrm{d}}{\mathrm{d}t}\int_V \tilde{\phi}_d \,\mathrm{d}V = \int_{\partial V}\left(\tilde{\phi}_d\tilde{\mathbf{u}}_d - \frac{1}{ScRe}\nabla\tilde{\phi}_d\right)\cdot(-\mathbf{n})\,\mathrm{d}A, \qquad (20)$$

where $\mathbf{n}$ is the surface outward normal and ∂V is the computational domain boundary. Here the first terms in the brackets on the right hand side corresponds to the convective flux of particles while the second term is the diffusive flux and together they account for the total flux of particles through the boundaries of the domain. At the top and bottom walls due to no-slip and no-penetration conditions $\tilde{\mathbf{u}}_d = \widetilde{\mathbf{V}}_s$ and thus the boundary condition Eq. (19) at the top wall corresponds to zero net flux of particles. At the bottom wall, since the concentration gradient is set to zero, the net flux of particles is due to settling of particles. Thus here we consider a depositional flow, where the net concentration of particles within the computational domain continually decreases due to the depositional flux of particles through the bottom boundary. In many physical situations there can be shear and turbulence induced resuspension of particles from the bottom boundary. Empirical models of resuspension yield a non-zero diffusive flux of particles at the boundary expressed as a function of wall shear and particle Reynolds number (García et al., 1993). In this work, as the first step towards understanding the role of particle inertia, we will avoid such empiricism and ignore resuspension of particles.

The solution of the concentration equation, even in the limit of a scalar field, can lead to sharp concentration gradients when diffusive effects are not adequately accounted for in spectral methods. In order to avoid resulting numerical difficulties, the Schmidt number of the scalar field is typically limited to $O(1)$. In the context of particulate concentration, the velocity of particle advection, $\mathbf{u}_d$, is different from the fluid velocity. More importantly, even though $\nabla\cdot\mathbf{u}_c = 0$, the corresponding divergence of particle velocity field will not be zero in case of inertial particles (i.e. if $\tilde{\tau} \neq 0$). This non-zero divergence of particle velocity field results in preferential accumulation of particles in regions of high strain-rate and avoidance of regions of high vorticity. Strong accumulation of particles is observed even at moderate values of $\tilde{\tau}$ (~ 0.025) resulting in even sharper gradients. Thus the importance of the diffusion terms is enhanced in the case of particulate concentrations.

Tadmor (1989) and Karamanos and Karniadakis (2000) have shown that spurious numerical behavior of the solution can be controlled by the use of a spectral viscosity without sacrificing spectral accuracy. In this approach, diffusion is increased for high wavenumbers to avoid Gibb's oscillations, but the effect on the large scales (small wavenumbers) is minimized. However, since the flow has a predominant flow direction, numerical instabilities have been observed to more likely occur in the direction of spreading than in the vertical direction, suggesting that an anisotropic implementation is needed. Based on these observations, following (Karamanos and Karniadakis, 2000 and Rani and Balachandar, 2003) the conservation of mass for the disperse phase is modified to

$$\frac{\partial\tilde{\phi}_d}{\partial\tilde{t}} + \nabla(\tilde{\phi}_d\tilde{\mathbf{u}}_d) = \frac{1}{Re\,Sc}\left[\frac{\partial}{\partial\tilde{x}}\left(Q_{k_x}\otimes\frac{\partial\tilde{\phi}_d}{\partial\tilde{x}}\right) + \frac{\partial^2\tilde{\phi}_d}{\partial\tilde{z}^2}\right]. \qquad (21)$$

Here Q_{k_x} is a wavenumber dependent diffusivity kernel and $\otimes$ denotes the convolution operation in physical space., i.e.

$$\frac{\partial}{\partial\tilde{x}}\left(Q_{k_x}\otimes\frac{\partial\tilde{\phi}_d}{\partial\tilde{x}}\right) = -\sum_{k_x} k_x^2\,\hat{Q}_{k_x}\hat{\phi}_d\exp(ik_x x) \qquad (22)$$

where $\hat{}$ represents the Fourier coefficient and $k_x = -N_x/2, \ldots, N_x/2-1$ is the wavenumber along the horizontal direction. The diffusivity kernel is computed as:

$$\widehat{Q}_{k_x} = \begin{cases} 1 & \text{for } |k_x| \leqslant M \\ 1 + (Sc/Sc_{sv})\exp\left[\left(k_x^2 - N_x^2/4\right)/\left(k_x^2 - M^2\right)\right] & \text{for } |k_x| > M. \end{cases} \qquad (23)$$

where Sc_{sv} and $M < N_x/2$ are free parameters to be selected. Based on numerical considerations we have chosen $Sc = 0.7$, and, in agreement with the findings of Härtel et al. (2000), Cantero et al. (2007a), Cantero et al. (2007b), we also observe that the results to be presented are not sensitive to this choice as long as Sc is kept order 1. Any attempt to control numerical oscillations by setting Sc smaller than order 1 results in over diffusive solutions where vortex shedding and Kelvin–Helmholtz instabilities are strongly damped. Several numerical test were performed to select adequate values for the diffusivity kernel. The optimal choice that yields the highest quality result is $Sc_{sv} \sim 3\times10^{-4}N_x$, $M \sim N_x/16$.

The numerical scheme requires the computation of the material derivative of the continuous phase velocity, $D_c\mathbf{u}_c/Dt$, at each time step to be used in the equilibrium approximation for the disperse phase velocity field (see Eq. (5)). The most stable, efficient and accurate way of computing this material derivative was employing a third order explicit approximation based on the continuous phase velocity over the four previous stages.

5. Results and discussion

First we explore the effect of inertia in isolation, without any gravitational settling of particles, by setting $\widetilde{V}_s = 0$. Although this is an idealized case, it can be considered as the limiting case of small heavy particles for which $\widetilde{V}_s/\tilde{\tau} \to 0$. In the second part of the results section we include settling effects and explore the influence of particle inertia on deposition patterns.

5.1. Front velocity

The height of the heavy current, $\tilde{h}$, as a function of the streamwise location can be defined as

$$\tilde{h}(\tilde{x},\tilde{t}) = \int_0^1 \tilde{\phi}_d(\tilde{x},\tilde{z},\tilde{t})\,\mathrm{d}\tilde{z}. \tag{24}$$

Thus at locations entirely occupied by the heavy particle laden fluid the current height will be 1.0 and in regions of pure fluid devoid of suspended particles the current height will be zero. The streamwise location of the current front, $\tilde{x}_F$, can be unambiguously defined as the point where the current height, $\tilde{h}$, reaches zero. In practice, although $\tilde{h}$ remains quite small, it does not become identically zero ahead of the current front due to diffusion. As a result a small threshold is used to identify the front location and the results are insensitive to the precise choice of the threshold (see details of definition in Cantero et al., 2007b). The front velocity can then be computed as

$$\tilde{u}_F = \frac{\mathrm{d}\tilde{x}_F}{\mathrm{d}\tilde{t}}. \tag{25}$$

Fig. 2 shows the time evolution of the front velocity for three different values of $\tilde{\tau} = 0$, 0.025 and 0.05 at $Re = 3450$. Three regimes can be clearly distinguished in this figure, an initial acceleration phase, followed by a constant velocity phase, and a final phase of decay. Cantero et al. (2007b) presented a detailed analysis of these velocity phases in the context of scalar currents (i.e. $\tilde{\tau} = 0$ and $\widetilde{V}_s = 0$). The current rapidly accelerates from its initial rest state and reaches a peak velocity at a dimensionless time of about $\tilde{t} \sim 1$.

It is interesting to note that during this initial acceleration phase the inertia of the suspended particles does not seem to make a large difference on the front velocity of the current. A close-up of the front velocity during the acceleration phase is shown in Fig. 2 as an inset. It can be seen that at the very early stages the inertia of the suspended particles tends to slow the current, which can be explained by noticing that as the current accelerates from the gate $D_c\tilde{\mathbf{u}}_c/D\tilde{t}$ is positive and, from Eq. (11), the streamwise velocity of the particles can be estimated to lag behind the fluid. From the inset it is also observed that at the later stages of acceleration the inertia of the particles tend to speed up the front and as a result the peak front velocity attained by the particulate current appears to be insensitive to $\tilde{\tau}$.

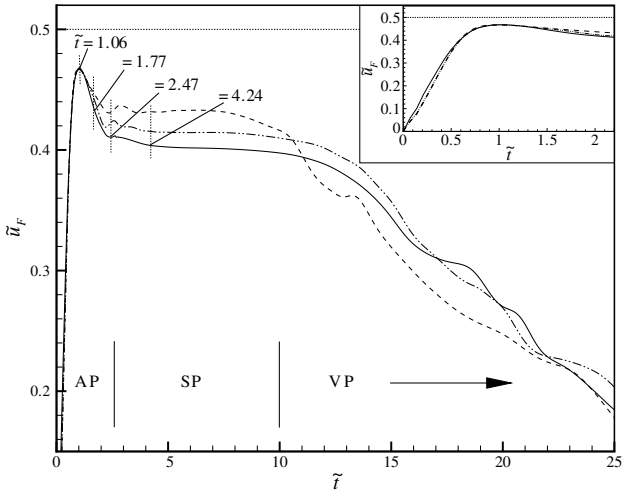

Fig. 2. Front velocity as a function of time for $\widetilde{V}_s = 0$. Solid line: $\tilde{\tau} = 0$, dash-dot line: $\tilde{\tau} = 0.025$ and dash line: 0.05. In the figure AP: acceleration phase, SP: slumping phase, and VP: viscous phase. Observe in the inset frame that during the initial acceleration phase the fronts corresponding with particulate front move slightly slower than the scalar case due to the inertial correction.

The inertial correction, $-\tilde{\tau}D\tilde{\mathbf{u}}/D\tilde{t}$, can be observed in Fig. 3 for $\tilde{t} = 1.77$. Fig. 3a shows contours of the carrier fluid horizontal velocity (solid line) together with the horizontal component of the particles velocity (dash line). The thick long-dash line is the contour of $\tilde{\phi}_d = 0.5$ and gives an indication of the front location. Fig. 3b shows the horizontal component of the inertial correction $-\tilde{\tau}D\tilde{\mathbf{u}}/D\tilde{t}$ (solid lines), and inertial correction vector field. At this time there is increased difference between the horizontal component of the fluid velocity and particles velocity as shown in frame (a). In frame (b) the vector field shows clearly the non-solenoidal nature of the inertial correction with the vector field converging at the top and bottom fronts. Observe that this convergence of the velocity field implies injection of particles into the heavy front at the bottom, which breaks the symmetry of the problem shown by the $\tilde{\phi}_d = 0.5$ line. The divergence of the inertial correction vector field is related to the newly formed Kelvin–Helmholtz vortices at the heavy and light fronts. As will be explained later, particles migrate from vortical regions and accumulate along regions of high shear.

Following the peak velocity the propagation of the current somewhat slows down before reaching a near constant front velocity. This deceleration of the current has been observed to coincide with roll up of the interfacial shear layer between the heavy and light fluids into coherent vortices. In the context of a scalar current it was observed (Cantero et al., 2007b) that the incipient roll up of the Kelvin–Helmholtz vortices started at around $\tilde{t} \sim 1$ and was nearly complete by $\tilde{t} \sim 2.5$. Fig. 4 shows contours of swirling strength at four time instances $\tilde{t} = 1.06$, 1.77, 2.47 and 4.24, which are also indicated in Fig. 2. Here the swirling strength, $\tilde{\lambda}_{ci}$, is defined as the absolute value of the imaginary portion of the complex eigenvalues of the local velocity gradient tensor.[1] Frame (a) of this figure shows the results for $\tilde{\tau} = 0.0$, frame (b) the results for $\tilde{\tau} = 0.025$ and frame (c) the results for $\tilde{\tau} = 0.05$. The values of peak swirling strength for the dominant vortices are indicated. During the deceleration subphase (at $\tilde{t} = 1.06$, 1.77 and 2.47), the interface roll-up produces strong Kelvin–Helmholtz vortices, which

[1] The local velocity gradient tensor has three eigenvalues. If all three eigenvalues are real then locally the flow is not swirling and $\tilde{\lambda}_{ci}$ is set to zero. If the local velocity gradient tensor has one real and a complex conjugate pair of eigenvalues, the imaginary part of the complex eigenvalue provides a clean measure of the local swirling strength (Zhou et al., 1999; Chakraborty et al., 2005).

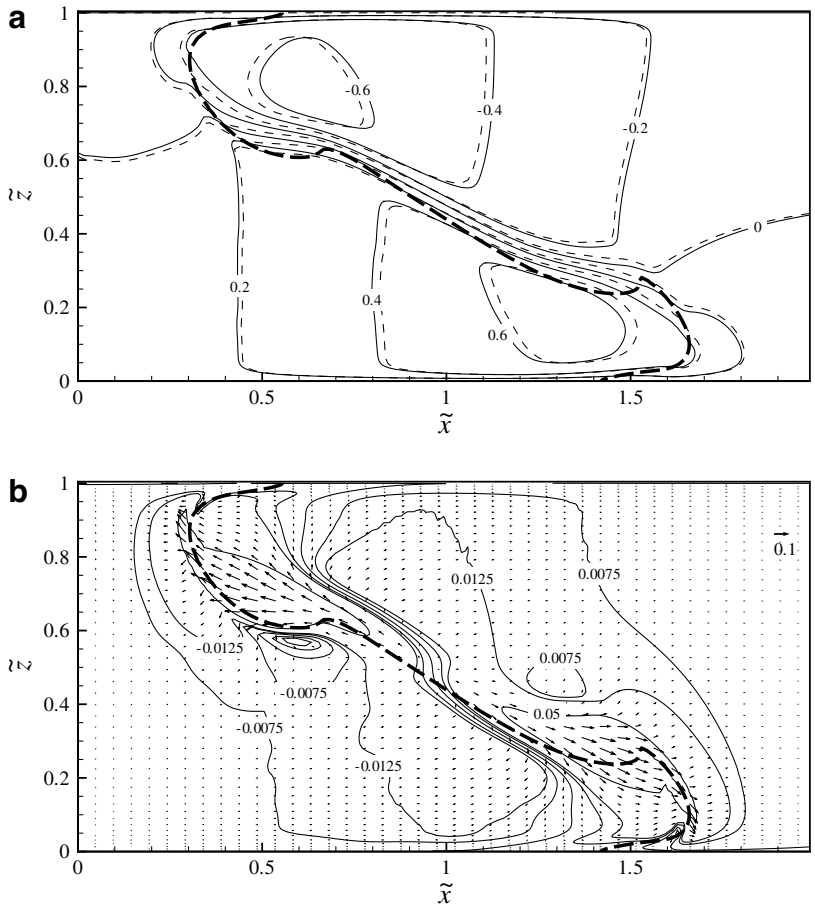

Fig. 3. Frame (a) horizontal component of fluid velocity (solid line) and particles velocity (dash line) for $\tilde{\tau} = 0.05$ and $\tilde{V}_s = 0.0$ at $\tilde{t} = 1.77$. The thick long-dash line is the contour of $\tilde{\phi}_d = 0.5$ and gives an indication of the front location. Frame (b) inertial correction $-\tilde{\tau} D\tilde{\mathbf{u}}/D\tilde{t}$ for $\tilde{\tau} = 0.05$ and $\tilde{V}_s = 0.0$ at $\tilde{t} = 1.77$. Contour lines for horizontal component of the inertial correction. The vector field shows the non-solenoidal nature of the inertial correction.

seem to regulate the value of the constant velocity of spreading in the slumping phase. With the presence of inertial particles the strength of the rolled up vortices weakens as indicated by the values of swirling strength during the deceleration subphase. This can perhaps be explained by the fact that inertial particles lag the fluid and cannot spin at the same rate of fluid elements. The consequence is a reduction in the deceleration rate.

Following the acceleration–deceleration phase the current settles to a near constant velocity in the slumping phase. The front velocities during this phase are 0.407, 0.415 and 0.432 for $\tilde{\tau} = 0$, $\tilde{\tau} = 0.25$ and $\tilde{\tau} = 0.05$, respectively. Thus, for the largest inertial particles considered here the constant slumping phase velocity has increased by about 6.1%. Cantero et al. (2007b) observed the front velocity of a scalar current in the slumping phase to be well captured by 2D simulations, since the dominant rolled up Kelvin–Helmholtz vortices remain sufficiently behind of the front. This behavior can be expected to remain unaffected for the case of the particulate currents as well. In the present simulations the constant velocity slumping phase extends over only a short period due to the limited amount to heavy fluid released. In the case of a large-volume release the constant velocity phase will persist for a long duration and the increased front velocity in a particulate current can significantly alter the arrival time of the current. The increase in front velocity with increasing inertial effect of the particles is due to particle accumulation near the head of the current and will be discussed below.

At high enough Reynolds number the constant velocity slumping phase will transition to an inertial phase, where the dominant balance is between gravity and inertia. The asymptotic behavior of a scalar current in the inertial phase shows a slow decay in the front velocity as $\tilde{u}_F \sim \tilde{t}^{-1/3}$ (Fay, 1969; Hoult, 1972; Huppert and Simpson, 1980). The time of transition from constant velocity to a slow inertial decay can be estimated to be Cantero et al. (2007b)

$$\tilde{t}_{SI} = \frac{0.94\tilde{x}_0\tilde{h}_0}{F_{p,sl}^3}, \tag{26}$$

where $\tilde{h}_0$ and $\tilde{x}_0$ are the dimensionless height and half-length of the initial release and $F_{p,sl}$ is the approximate constant velocity of the front in the slumping phase. Thus, with increasing constant front velocity during the slumping

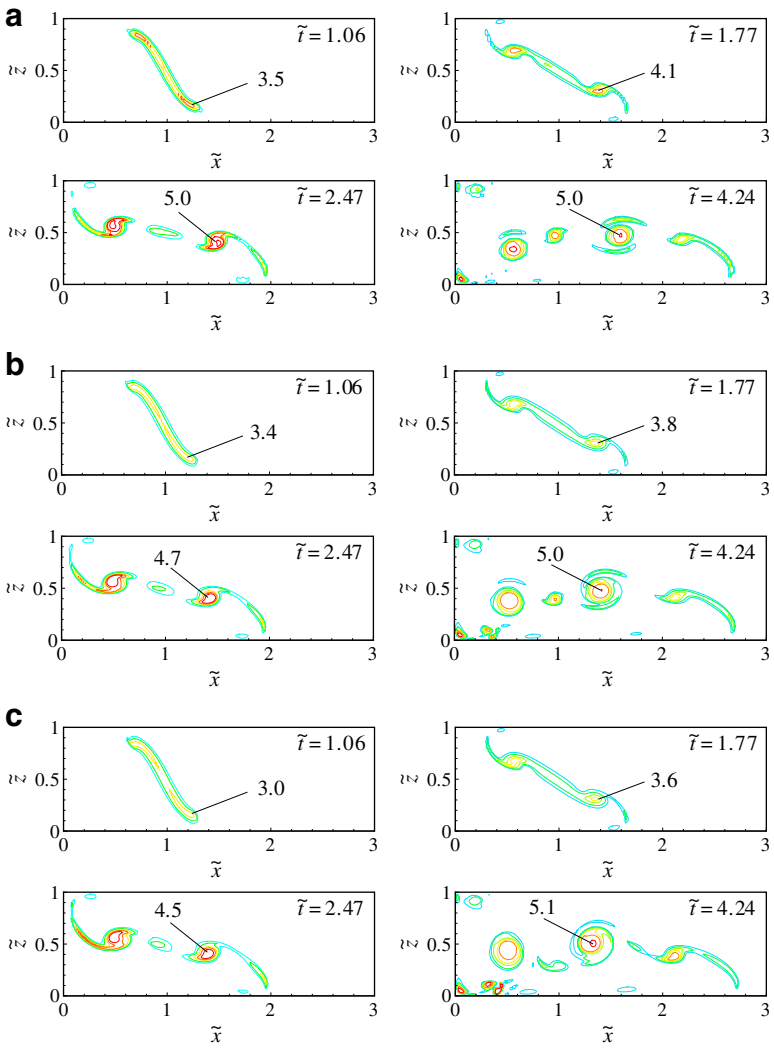

Fig. 4. Swirling strength during acceleration phase for $\widetilde{V}_s = 0.0$. Frame (a) $\tilde{\tau} = 0.0$, frame (b) $\tilde{\tau} = 0.025$ and frame (c) $\tilde{\tau} = 0.05$. The inset numbers indicate the swirling strength value for the main vortical structure as the front advances. Observe that for early times ($\tilde{t} \leqslant 2.47$) the strength of this vortex diminishes with the inertia of the particles.

phase, the transition to inertial phase occurs earlier. For the present case of $\tilde{h}_0 = \tilde{x}_0 = 1$ the slumping-to-inertial transition times can be estimated as $\tilde{t}_{SI} = 13.9$, 13.1 and 11.6 for the cases of $\tilde{\tau} = 0$, 0.025 and 0.05, respectively.

However, at lower current strengths (i.e. at lower Re) a direct transition from slumping to viscous phase will occur without going through an inertial phase (Cantero et al., 2007b). The transition time from slumping to viscous phase can be estimated as

$$\tilde{t}_{SV} = \frac{0.57(\tilde{h}_0\tilde{x}_0)^{3/4}}{F_{p,sl}^{5/4}} Re^{1/4}. \tag{27}$$

Here again the transition will occur earlier with increasing constant front velocity during the slumping phase. For the three $\tilde{\tau} = 0$, 0.025 and 0.05 cases the transition times can be estimated as $\tilde{t}_{SV} = 13.5$, 13.1 and 12.5. Thus, for the present modest Re, the estimated slumping to viscous transition times are very close to the slumping to inertia transition times. In fact, simple theoretical arguments show that for a full-depth planar current of unit initial release ($\tilde{h}_0 = \tilde{x}_0 = 1$) to enter the inertial phase the Reynolds number of release must be greater than $\sim 3.4 \times 10^3$ (Cantero et al., 2007b). The $Re = 3450$ of the present simulation is clearly in the critical range and as a result if an inertial phase were to exist its extent will be quite limited and the current can be expected to transition quickly to the viscous phase. The transition times observed in Fig. 2 are in reasonable agreement with the theoretical estimates for the cases of $\tilde{\tau} = 0$ and 0.025. For the larger inertial particles, the computed transition from the slumping phase is observed to occur somewhat earlier. Clearly the theoretical predictions are for a scalar current and they do not account for the inertial effect of particles. In the viscous phase the front velocity of both the scalar and the particulate currents are observed to decay at about the same rate. Although, the velocity for the $\tilde{\tau} = 0.05$ case is consistently a little lower than for the other two cases.

5.2. Preferential accumulation

The concentration Eq. (12) can be rewritten in the following form

$$\frac{D_d\tilde{\phi}_d}{D\tilde{t}} = \frac{1}{ScRe}\nabla^2\tilde{\phi}_d - \tilde{\phi}_d\nabla\cdot\tilde{\mathbf{u}}_d. \tag{28}$$

From which it can be seen that in a scalar current, where $\nabla\cdot\tilde{\mathbf{u}}_d = \nabla\cdot\tilde{\mathbf{u}}_c = 0$, at all later times the local concentration of scalar is guaranteed to be lower than the initial uniform concentration before release in the heavier fluid. This is however not the case for particulate currents, where the divergence of particle velocity can be non-zero. The equilibrium approximation provides a convenient way to obtain the divergence of particle velocity. By taking the divergence of Eq. (11) we obtain

$$\nabla\cdot\tilde{\mathbf{u}}_d = \tilde{\tau}(\|\boldsymbol{\Omega}_c\|^2 - \|\mathbf{S}_c\|^2), \tag{29}$$

where $\boldsymbol{\Omega}_c$ and $\mathbf{S}_c$ are the skew-symmetric and symmetric parts of the local fluid velocity gradient tensor, respectively. Note that $\mathbf{V}\tilde{\mathbf{u}}_d > 0$ when $\|\boldsymbol{\Omega}_c\| > \|\mathbf{S}_c\|$, which implies that particles migrate from regions of vorticity and accumulate in regions of high strain-rate. This preferential migration of particles increases with increasing $\tilde{\tau}$.

Fig. 5 shows the structure of the current in the scalar limit ($\widetilde{V}_s = 0$ and $\tilde{\tau} = 0$) at four different time instances. The flow is visualized by contours of particle concentration. Soon after release an intrusion front forms with a lifted nose due to the no-slip boundary condition. As the current advances Kelvin–Helmholtz vortices form at the interface, which together with bottom drag, balances the initial acceleration of the heavy front. As a consequence, after the initial set-up of the Kelvin–Helmholtz vortices, the front moves at constant speed until dilution and viscous effects in the current become important. Then, the current slows down and eventually dissipates.

Figs. 6 and 7 show the corresponding results for currents with inertial particles of negligible settling, that is for $\tilde{\tau} = 0.025$ and $\tilde{\tau} = 0.05$ with $\widetilde{V}_s = 0$. The solid lines indicate contours of $\tilde{\phi}_d \leqslant 1$, and dash lines correspond to $\tilde{\phi}_d \geqslant 1$. Particulate currents differ from their scalar counterpart in several ways. First, regions of $\tilde{\phi}_d \geqslant 1$ are not present in the scalar current as can be expected on theoretical grounds. In contrast, significant regions of $\tilde{\phi}_d \geqslant 1$ can be observed in case of particulate currents. At early times ($\tilde{t} < 10$) these regions of increased concentration can be observed to extend right behind the head of the current. This provides support for the sustained increase in the constant velocity of the particulate current in the slumping phase. At later times, when the current enters the inertial and viscous phases, such enhanced concentrations are not observed and accordingly the propagation of the particulate currents is not faster.

Also shown in Figs. 5–7 at early times are the particle concentration levels at the center of the rolled up Kelvin–Helmholtz vortices. It is clear that with particle inertia the concentration of particles at the cores of the vortices has reduced to zero. Particles, owing to their inertia, are expected to spin out of the coherent vortices resulting in vortex cores devoid of particles. In contrast to these vortex cores, the body of the current, below the vortex cores, correspond to regions of high strain-rate and thus constitutes regions where particles accumulate. Also, due to particle inertia, long tongues of heavy particle laden fluids can be seen to extend above the body of the current. Such flow features can be expected to have an impact on instantaneous wall shear stress and deposition patterns.

Fig. 8 shows the vertical profile of streamwise-averaged particle concentration at $\tilde{t} = 2.47$ defined as

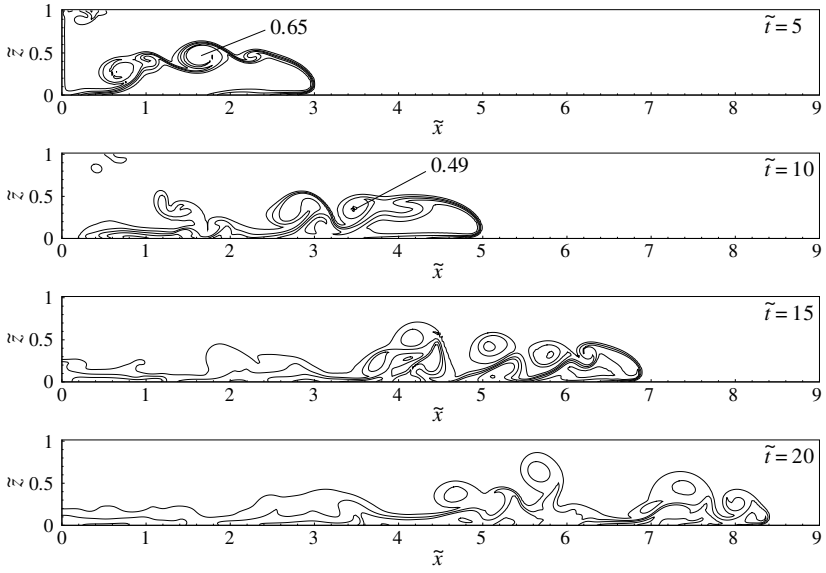

Fig. 5. Contours of particles concentration. Solid line: $0.1 < \tilde{\phi}_d < 1$, dash line: $1.0 < \tilde{\phi}_d$. Solution for $\tilde{\tau} = 0$ and $\widetilde{V}_s = 0$. Inset numbers indicate local value of $\tilde{\phi}_d$.

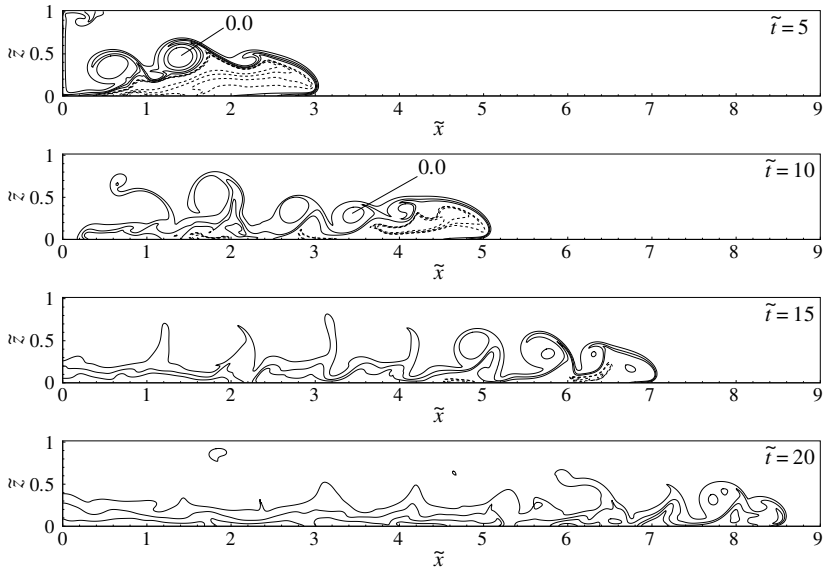

Fig. 6. Contours of particles concentration. Solid line: $0.1 < \tilde{\phi}_d < 1$, dash line: $1.0 < \tilde{\phi}_d$. Solution for $\tilde{\tau} = 0.025$ and $\widetilde{V}_s = 0$. Inset numbers indicate local value of $\tilde{\phi}_d$. Observe that particles migrate from the vortex cores (compare inset values to Fig. 5) to accumulate into the front of the current. The structure of the current is slightly changed at later times compared to the case of $\tilde{\tau} = 0$ and $\widetilde{V}_s = 0$ (see Fig. 5).

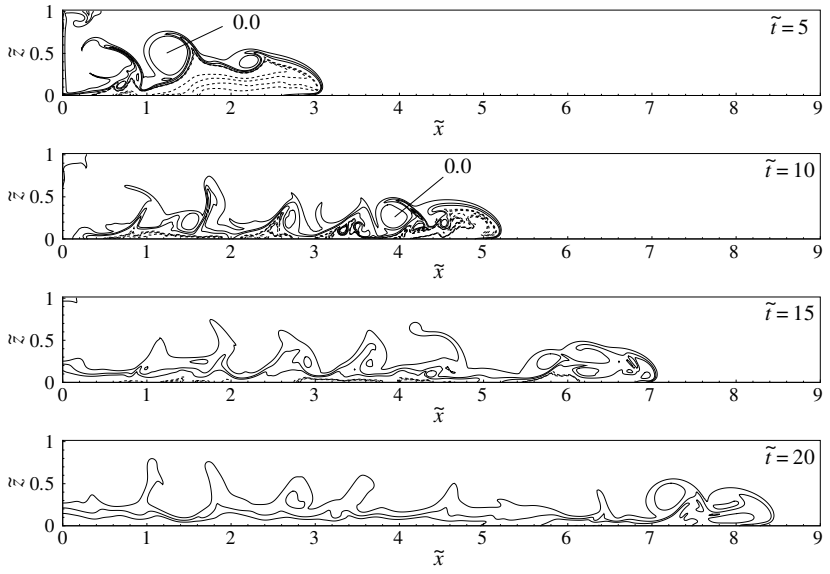

Fig. 7. Contours of particles concentration. Solid line: $0.1 < \tilde{\phi}_d < 1$, dash line: $1.0 < \tilde{\phi}_d$. Solution for $\tilde{\tau} = 0.05$ and $\widetilde{V}_s = 0.0$. Inset numbers indicate local value of $\tilde{\phi}_d$. Observe that particles migrate from the vortex cores (compare inset values to Fig. 5) to accumulate into the front of the current. The structure of the current is changed for $\tilde{t} \geqslant 10$ compared to the case of $\tilde{\tau} = 0$ and $\widetilde{V}_s = 0$ (see Fig. 5).

$$\tilde{\phi}_d^{(x)}(\tilde{z},\tilde{t}) = \frac{1}{\widetilde{L}_x/2}\int_0^{\widetilde{L}_x/2} \tilde{\phi}_d(\tilde{x},\tilde{z},\tilde{t})\mathrm{d}\tilde{x}. \tag{30}$$

The currents with inertial particles present a larger mean particle concentration for $\tilde{z} < 0.3$, where the front of the current is located. The concentration of particles over the region $0.3 < \tilde{z} < 0.6$ is lower for the inertial particles, since this is where the vortices are located and the particles are spun out of their cores. The relative difference between the maximum values of $\tilde{\phi}_d$ for $\tilde{\tau} = 0.0$ and $\tilde{\tau} = 0.05$ is about 5%. However, it is observed from Figs. 6 and 7 that the increase in concentration is not distributed uniformly along the horizontal direction, but preferentially close to the head of the current. This localized increase in concentration is likely to be the main source of the 6% increase in the front velocity observed in the slumping phase.

In the initial acceleration phase particles do not affect substantially the flow structure compared to the scalar case. Once Kelvin–Helmholtz vortices start forming (at the beginning of the deceleration subphase), inertial particles resist spinning as fast as the carrier fluid, and on

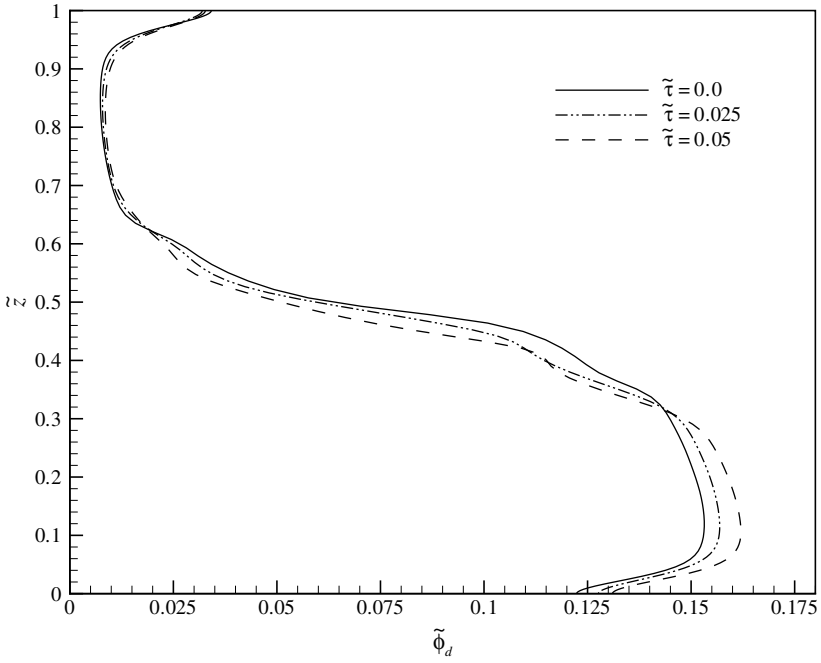

Fig. 8. Mean vertical particle concentration $\left(\tilde{\phi}_d^{\langle x \rangle}\right)$ profile for $\widetilde{V}_s = 0.0$ at $\tilde{t} = 2.47$. Solid line $\tilde{\tau} = 0.0$, dash-dot line $\tilde{\tau} = 0.025$, and dash line $\tilde{\tau} = 0.05$. Particles spun out of the interface Kelvin–Helmholtz vortices ($0.3 \leqslant \tilde{z} \leqslant 0.6$) accumulate in the head and body of the current ($\tilde{z} \leqslant 0.3$).

average diminish the initial strength of interface roll up. This scenario of weaker interfacial vortices for the inertial particles is accurate only in the deceleration subphase, and soon changes in the constant velocity slumping phase. The net circulation at the interface can be estimated as (Cantero et al., 2007a)

$$\Lambda(\tilde{t}) \sim \tilde{u}_F \tilde{x}_F. \tag{31}$$

Thus in the constant velocity slumping phase circulation increases linearly with time with the slope given by the front velocity. With the higher front velocity, the net circulation at the interface for the inertial particles is higher than that for the corresponding scalar case (non-inertial particles). Fig. 9 shows the swirling strength for time $\tilde{t} = 10$. Frame (a) shows the results for $\tilde{\tau} = 0.0$ with $\widetilde{V}_s = 0.0$, frame (b) shows the results for $\tilde{\tau} = 0.025$ with $\widetilde{V}_s = 0.0$ and frame (c) shows the results for $\tilde{\tau} = 0.05$ with $\widetilde{V}_s = 0.0$. The correspondence between the locations of intense vortices as seen in the swirling strength contours and the regions devoid of particles in the concentration contours confirm the role of intense vortices. Consistent with the estimate for interfacial circulation, the extent of vortical region observed for the $\tilde{\tau} = 0.05$ case is much larger than the $\tilde{\tau} = 0.0$ case. Also in the case of inertial particles, rolled up vortices can be observed to penetrate all the way up to the front of the current, while in the scalar case, the

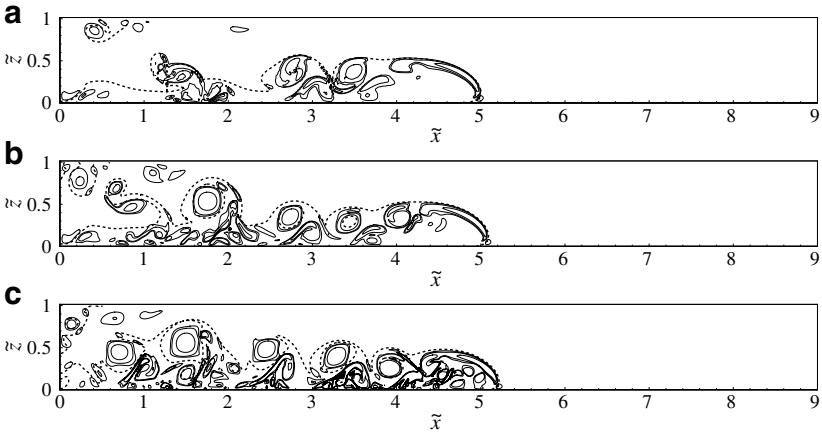

Fig. 9. Contours of $\tilde{\lambda}_{ci}$ (solid line) for $\tilde{t} = 10$. Dash line is the contour for particle concentration $\tilde{\phi}_d = 0.05$. Frame (a) shows the solution for $\tilde{\tau} = 0$ and $\widetilde{V}_s = 0.0$, frame (b) shows the solution for $\tilde{\tau} = 0.025$ and $\widetilde{V}_s = 0.0$, and frame (c) shows the solution for $\tilde{\tau} = 0.05$ and $\widetilde{V}_s = 0.0$. At the instant shown, case (c) shows increased vortical activity in the front and body of the current.

rolled up vortices are located away from the front. It has been argued that the dynamic low pressure associated with the coherent vortices that are located close to the front of the current lowers the driving horizontal pressure gradient and thereby reduce the speed of the current (Cantero et al., 2007a). Thus, despite the presence of coherent vortices close to the front, the increased velocity of the current with inertial particles, indicates the important role of particle accumulation close to the front.

At a much later time of $\tilde{t} = 20$, the current with $\tilde{\tau} = 0.05$ presents a somewhat lower vortical activity in the near-front region, while the currents with $\tau = 0.025$ and $\tilde{\tau} = 0.0$ show relatively stronger vortical activity near the front of the current as seen in Fig. 10. This figure presents the same information as Fig. 9 at the later time of $\tilde{t} = 20$. In the viscous phase self similar theories predict the front velocity to be either $\tilde{u}_F \sim \tilde{t}^{5/8}$ or $\tilde{u}_F \sim \tilde{t}^{4/5}$ depending on the relative importance of interfacial vs bottom wall friction (Hoult, 1972; Huppert, 1982). From (31), using either of the power laws for the front velocity, it can be estimated that in the viscous phase net circulation at the interface decreases with time and thus formation of new vortices

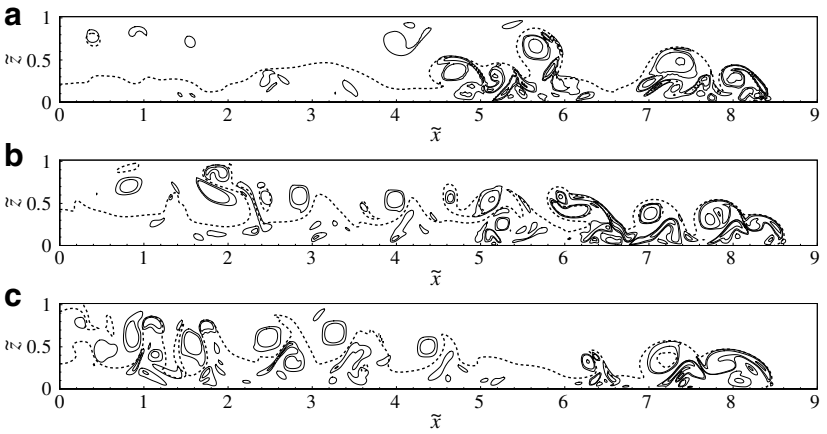

Fig. 10. Contours of $\tilde{\lambda}_{ci}$ (solid line) for $\tilde{t} = 20$. Dash line is the contour for particle concentration $\tilde{\phi}_d = 0.05$. Frame (a) shows the solution for $\tilde{\tau} = 0$ and $\widetilde{V}_s = 0.0$, frame (b) shows the solution for $\tilde{\tau} = 0.025$ and $\widetilde{V}_s = 0.0$, and frame (c) shows the solution for $\tilde{\tau} = 0.05$ and $\widetilde{V}_s = 0.0$. At the instant shown the main difference is at the tail of the current (left half of the figures), where there is increased vortical activity with increasing particle inertia.

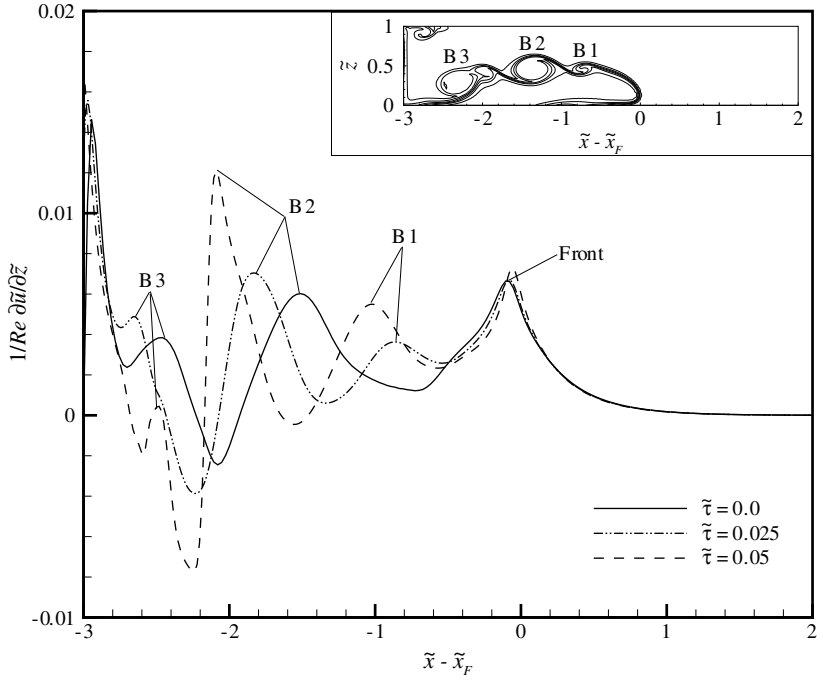

Fig. 11. Dimensionless bed shear stress for $\widetilde{V}_s = 0$ at $\tilde{t} = 5$ after the currents have traveled about 3 dimensionless length units. Solid line: $\tilde{\tau} = 0$, dash-dot line: $\tilde{\tau} = 0.025$, and dash line: $\tilde{\tau} = 0.05$. The inset shows the current structure for $\tilde{\tau} = 0$ visualized by particle concentration contours. Three vortical structures are identified as B1, B2 and B3.

is not expected. The increased level of coherent vortices in the $\tilde{\tau} = 0.0$ and $\tilde{\tau} = 0.025$ cases near the front is consistent with the higher current speed observed for these cases during the viscous decaying phase. Also, in these cases, the strong interaction between the vortices at the front of the current results in episodic increase and decrease in the current speed, which can be observed in Fig. 2 as undulations.

5.3. Bottom shear stress

The shear stress distribution at the bottom boundary plays an important role in the resuspension of particles and thus in the time evolution of bed morphology. Fig. 11 shows the dimensionless bed shear stress, $(1/Re)\partial\tilde{u}_c/\partial\tilde{z}$, at $\tilde{t} = 5$ when the front of the current is located at $\tilde{x} \simeq 3$ for the three simulations of different particle inertia. The inset in the figure shows the instantaneous structure of the current visualized by concentration contours for the case of $\tilde{\tau} = 0$. The overall structure of the current is similar for the other two cases as well (see Figs. 5–7).

As is evident from the figure, considerable variation can be observed in the local shear stress distribution. The peak located at $\tilde{x} \sim \tilde{x}_F$ in Fig. 11 is associated with the front. The subsequent three peaks are associated with the vortices identified in the inset as B1, B2 and B3. In the case of the scalar current the peak associated with the vortex B1

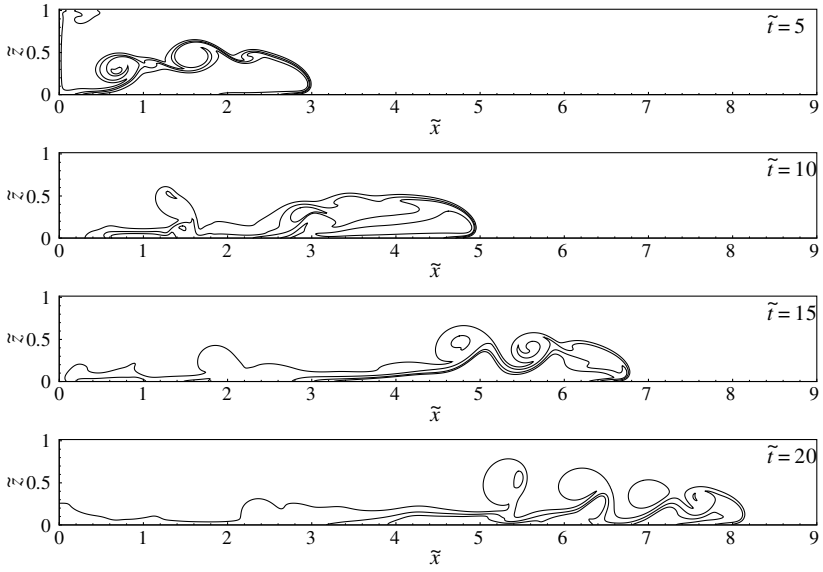

Fig. 12. Contours of particles concentration. Solid line: $0.1 < \tilde{\phi}_d < 1$, dash line: $1.0 < \tilde{\phi}_d$. Solution for $\tilde{\tau} = 0$ and $\tilde{V}_s = 0.005$. The flow is shallower and slower due to particle settling (compare to structure and front location in Fig. 5).

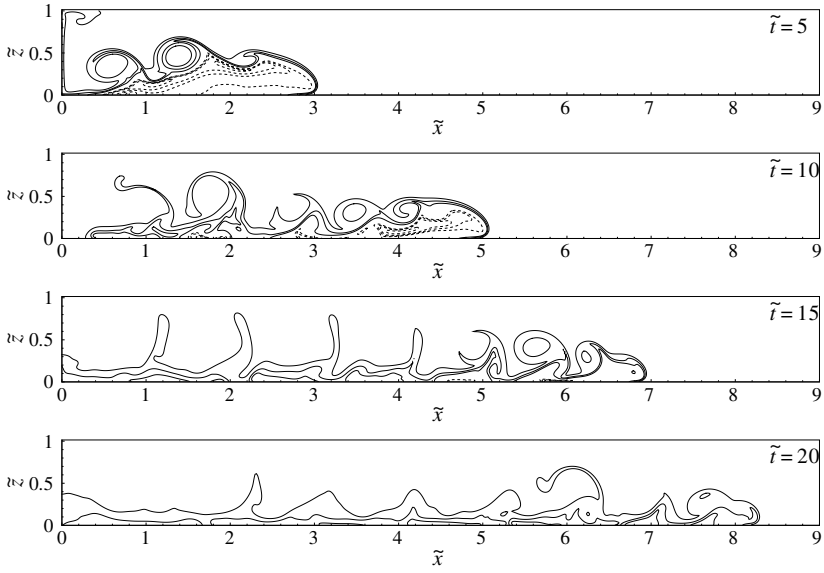

Fig. 13. Contours of particles concentration. Solid line: $0.1 < \tilde{\phi}_d < 1$, dash line: $1.0 < \tilde{\phi}_d$. Solution for $\tilde{\tau} = 0.025$ and $\tilde{V}_s = 0.005$. The flow is shallower and slower due to particle settling (compare to structure and front location in Fig. 6).

is weak because the billow B1 has not grown strong enough. The stronger vortices for the cases of $\tilde{\tau} = 0.025$ and $\tilde{\tau} = 0.05$ with the inertial particles are responsible for the larger values of bed shear stress. With increasing inertial effect of the particles the vortices B1, B2 and B3 move farther away from the front, but contribute to increased variation in the wall shear stress. Such differences in the bottom shear stress distribution persists at later time instances as well.

5.4. Effect of particle settling

Figs. 12–14 show the structure of the current for the three different inertial effects ($\tilde{\tau} = 0$, 0.025 and 0.05), respectively, but for the case of weak particle settling given by $\widetilde{V}_s = 0.005$. At early times ($\tilde{t} < 15$) the net loss of particles due to sedimentation is not significant to greatly alter the dynamics of the flow. The observed flow structures at these early times are quite similar to those observed without any settling effect. Thus the role of particle inertia persists with the presence of weak gravitational settling. At later times, however, the loss of particles through settling is sufficiently significant that the current looses its intensity and begins to die quite rapidly. As can be expected, even weak particle settling has a dramatic effect at long times. Simulations with larger settling effects are uninteresting as the current dies off too quickly. In reality, settling of particles must be balanced by resuspension of particles, and in this limit the effect of particle settling in the bulk of the current can be of interest.

The net instantaneous deposition of particles at the bottom boundary can be defined as

$$\dot{\tilde{m}}_s(\tilde{t}) = \int_0^{\widetilde{L}_x} \widetilde{V}_{sz}\,\tilde{\phi}_d(\tilde{x}, \tilde{z} = 0, \tilde{t})\,\mathrm{d}\tilde{x} \tag{32}$$

and the results computed for the three different values of $\tilde{\tau}$ is presented in Fig. 15. Up to $\tilde{t} \simeq 15$ the deposition rate increases. The increase is mainly due to the increase in planform area covered by the current. At later times, although the planform of the current continues to increase at a slower rate, the reduction in concentration is sufficiently large that net deposition decreases with time. Interestingly, as observed in Figs. 12–14, $\tilde{t} \simeq 15$ is about the time when the effect of particle settling begins to have a strong effect on the dynamics of the current. As can be seen from the figure, the net effect of inertia is to increase the deposition rate at early times. The deposition rate is increased due to the larger accumulation of particles in the body of the current ($\tilde{z} < 0.3$) as they are spun out of the vortices. At later times,

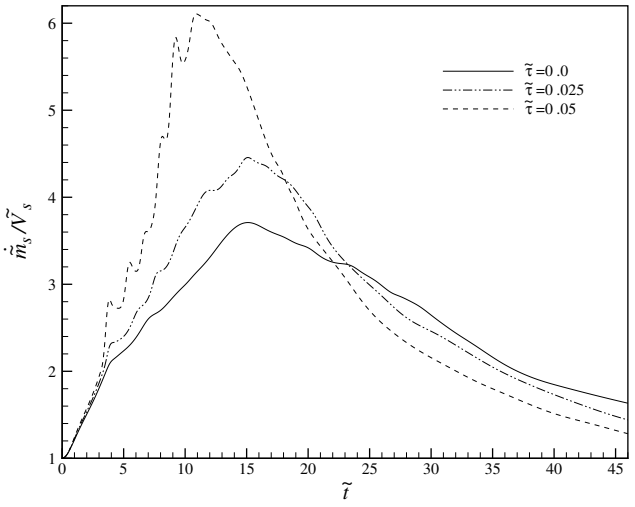

Fig. 15. Sediment deposition rate as a function of time for $\widetilde{V}_s = 0.005$. The net effect of inertia is to increase the deposition rate due to the larger accumulation of particles near the bottom.

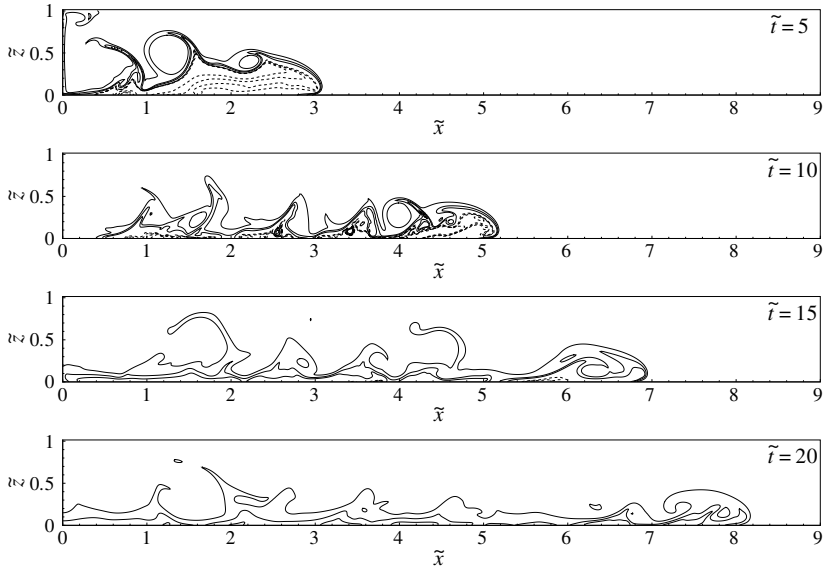

Fig. 14. Contours of particles concentration. Solid line: $0.1 < \tilde{\phi}_d < 1$, dash line: $1.0 < \tilde{\phi}_d$. Solution for $\tilde{\tau} = 0.05$ and $\widetilde{V}_s = 0.005$. The flow is shallower and slower due to particle settling (compare to structure and front location in Fig. 7).

due to increased reduction in the suspended mass of particles, the deposition rate for inertial particles decreases.

The cumulative deposition of particles can be computed as

$$\widetilde{D}(\tilde{x},\tilde{t}) = \int_0^{\tilde{t}} \widetilde{V}_{sz}\,\tilde{\phi}_d(\tilde{x}, z \tilde{=} 0, \hat{t})\,\mathrm{d}\hat{t}. \tag{33}$$

Fig. 16 shows $\widetilde{D}$ at three different time instances $\tilde{t} = 10$, 20 and 45 for the three different inertial particles. Frame (a) shows the results for $\tilde{\tau} = 0$, frame (b) for $\tilde{\tau} = 0.025$ and frame (c) for $\tilde{\tau} = 0.05$. As explained above, deposition is significantly enhanced by inertia. Not only the total deposition is increased but also the deposit pattern is substantially influenced. Preferential concentration of particles generate localized regions of increased deposition which explains the different peaks in frames (b) and (c). It is interesting to note for $\tilde{\tau} = 0.025$ a regular undulating pattern of enhanced and suppressed deposition is observed, which is somewhat less pronounced in the cases of no inertial effect and the largest inertial effect considered. It can also be observed that the spatial wavelength of the undulatory deposition pattern decreases with the increased inertial effect of the particles.

6. Summary and conclusions

We have presented simulations of particulate currents employing a two-phase flow model which includes both the settling and also the particle inertia effects. The model consists of conservation equations for the continuous phase, an algebraic equation for the particle velocity based on the equilibrium Eulerian approach (Ferry and Balachandar, 2001), and a transport equation for the particle volumetric concentration. By the incorporation of the equilibrium Eulerian approach we avoid solving additional differential equations for the conservation of particulate momentum, which constitutes a big saving in computational time.

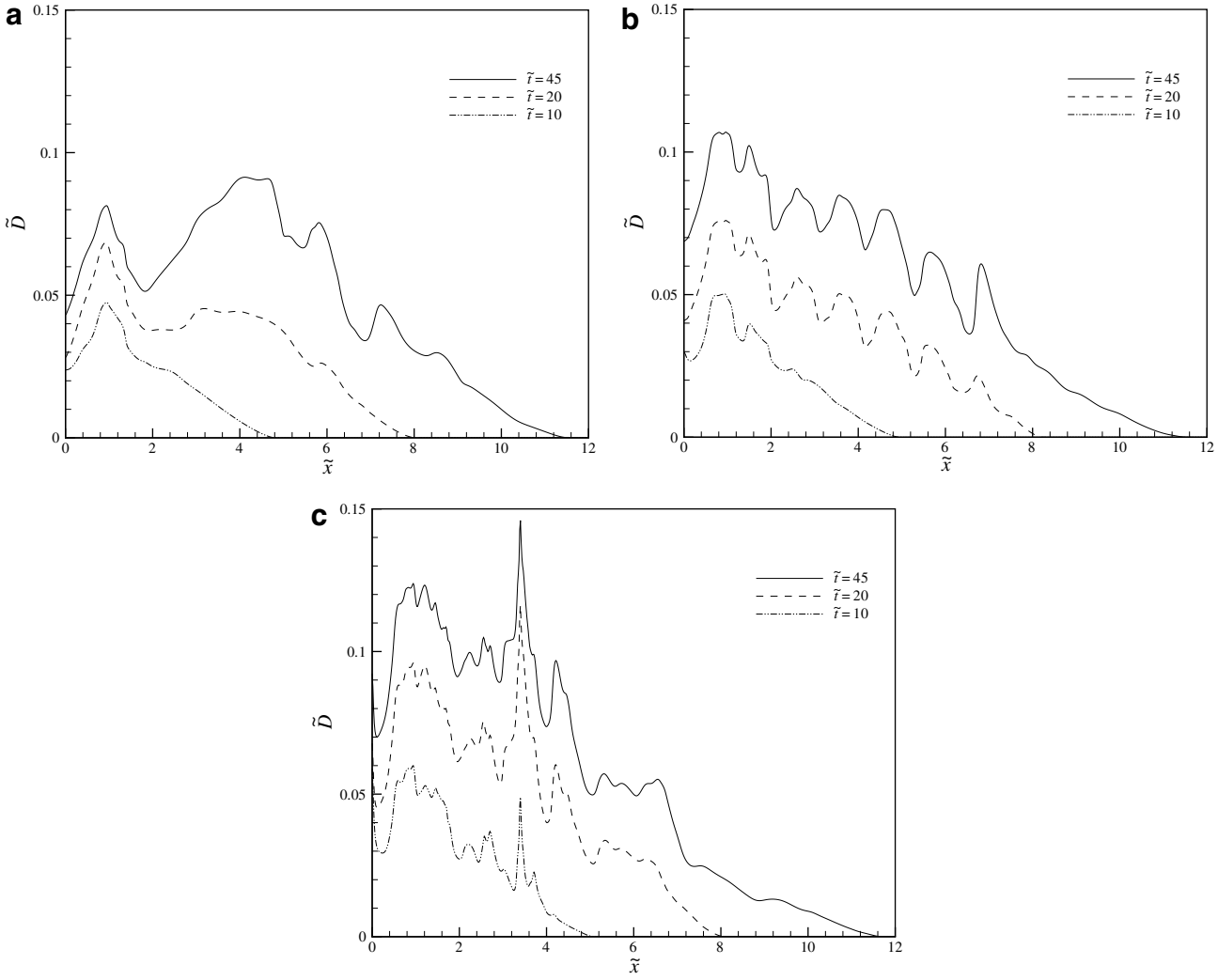

Fig. 16. A posteriori analysis of deposition (without resuspension included). The figure shows the influence of particle inertia on total deposition $\widetilde{D}$. The deposit is visualized for three time instants: $\tilde{t} = 10$, 20 and 45. Frame (a): $\widetilde{V}_s = 0.005$, $\tilde{\tau} = 0$. Frame (b): $\widetilde{V}_s = 0.005$, $\tilde{\tau} = 0.025$. Frame (c): $\widetilde{V}_s = 0.005$, $\tilde{\tau} = 0.05$.

The results presented in this work clearly show that particle inertia has an important influence on the structure and dynamics of the particulate currents. Particles migrate from the core of Kelvin–Helmholtz vortices and accumulate in the front and body of the current. As a result the concentration of particles near the front is observed to be even higher than the concentration in the original release. Such preferential concentration of particles at the front results in a measurable increase in the constant velocity of the current during the slumping phase. The level of increase in the constant slumping phase velocity increases with particle inertia. The change in the structure of the current modifies the vortex pattern and its intensity. As a consequence we observe the associated bottom shear stress to be more intense in the case of inertial particles. This can have a strong influence on erosion and resuspension of particles from the bed.

Particle inertia has a significant effect on the deposition rate. We observe local cumulative deposit to be more than 100% larger for the case of particles of weak inertia ($\tilde{\tau} = 0.05$) as compared to particles of negligible inertial effect ($\tilde{\tau} = 0.0$). This dramatic increase in the deposition rate is due to the preferential accumulation of particles closer to the wall ($\tilde{z} < 0.3$) as they are spun out of interfacial vortices. Not only the deposition rate is increased but also the deposition pattern is changed.

The present work focuses on flows with a single particle size while natural flows are commonly multi-size. The results presented here may have implications in deposits displaying layering patterns and longitudinal shorting produced by flow with multi-size particles. The focus of the present work is rather to introduce a novel Eulerian–Eulerian model where particle settling and inertia are taken into account. However, incorporating several particle sizes in the model is straightforward, and the analysis of such flows is left for future research.

Acknowledgements

We gratefully acknowledge the support of the Coastal Geosciences Program of the US Office of Naval Research grant N00014-93-1-0044, National Science Foundation grant EAR0609712, the Chicago District of the US Army Corps of Engineers, and the Metropolitan Water Reclamation District of Greater Chicago. Support from the National Center for Supercomputing Applications (NCSA) at the University of Illinois at Urbana-Champaign (UIUC) is also acknowledged. Mariano Cantero was supported by a Graduate Student Fellowship from the Computational Science and Engineering Program at UIUC. Dr. James Ferry collaborated in the early stages of the computations.

References

Acrivos, A., 1995. Bingham award lecture – 1994. Shear-induced particle diffusion in concentrated suspensions of noncolloidal particles. J. Rheol. 39 (5), 813–826.

Allen, J., 1985. Principles of Physical Sedimentology. George Allen and Unwin Ltd.

Altinakar, S., Graff, W., Hopfinger, E., 1990. Weakly depositing turbidity current on small slope. J. Hydra. Res. 28, 55–80.

Bagnold, R., 1962. Autosuspension of transported sediment; turbidity currents. Proc. Roy. Soc. London Ser. A 205.

Best, J., Kirkbride, A., Peakall, J., 2001. Mean flow and turbulence structure of sediment-laden gravity currents: new insight using ultrasonic Doppler velocity profiling. In: McCaffrey, B.K.W., Peakall, J. (Eds.), Particulate Gravity Currents. Blackwell Science, pp. 159–172.

Blanchette, F., Strauss, M., Meiburg, E., Kneller, B., Glinsky, M., 2005. High-resolution numerical simulations of resuspending gravity currents: condition for self-sustainment. J. Geophys. Res. 110, c12022.

Bonnecaze, R., Lister, J., 1999. Particle-driven gravity currents down planar slopes. J. Fluid Mech. 390, 75–91.

Bonnecaze, R., Huppert, H., Lister, J., 1993. Particle-driven gravity currents. J. Fluid Mech. 250, 339–369.

Bonnecaze, R., Hallworth, M., Huppert, H., Lister, J., 1995. Axisymmetric particle-driven gravity currents. J. Fluid Mech. 294, 93–121.

Brown, D., Cortez, R., Minion, M., 2001. Accurate projection methods for the incompressible Navier–Stokes equations. J. Comp. Phys. 168, 464–499.

Cantero, M., Balachandar, S., García, M., Ferry, J., 2006. Direct numerical simulations of planar and cyindrical density currents. J. Appl. Mech. 73, 923–930.

Cantero, M., Balachandar, S., García, M., 2007a. Highly resolved simulations of cylindrical density currents. J. Fluid Mech. 590, 437–469.

Cantero, M., Lee, J.R., Balachandar, S., García, M., 2007b. On the front velocity of gravity currents. J. Fluid Mech. 586, 1–39.

Canuto, C., Hussaini, M., Quarteroni, A., Zang, T., 1988. Spectral Methods in Fluid Dynamics. Springer-Verlag.

Chakraborty, P., Balachandar, S., Adrian, R., 2005. On the relationships between local vortex identification schemes. J. Fluid Mech. 535, 189–214.

Choi, S.-U., García, M., 1995. Modeling of one-dimensional turbidity currents with a dissipative-Galerkin finite element method. J. Hydra. Res. 33 (5), 623–648.

Cortese, T., Balachandar, S., 1995. High performance spectral simulation of turbulent flows in massively parallel machines with distributed memory. Int. J. Supercomput. Applicat. 9 (3), 187–204.

Crowe, C., Sommerfeld, M., Tsuji, Y., 1998. Multiphase flows with droplets and particles. CRC Press.

de Rooij, F., Dalziel, S., 2001. Time- and space-resolved measurements of deposition under turbidity currents. In: McCaffrey, W.B.K., Peakall, J. (Eds.), Particulate Gravity Currents. Blackwell Science, pp. 207–215.

Drew, D., Passman, S., 1998. Theory of multicomponent fluids. In: Applied Mathematical Sciences, vol. 135. Springer, New York.

Droegemeier, K., Wilhelmson, R., 1987. Numerical simulation of thunderstorm outflows dynamics. Part I: Outflow sensitivity experiments and turbulence dynamics. J. Atmospheric Sci. 44 (8), 1180–1210.

Fay, J., 1969. The spreads of oil slicks on a calm sea. In: Hoult, D.P. (Ed.), Oils in the sea. pp. 53–63.

Ferry, J., Balachandar, S., 2001. A fast Eulerian method for disperse two-phase flow. Int. J. Multiphase Flows 27, 1199–1226.

Ferry, J., Balachandar, S., 2002. Equilibrium expansion for the Eulerian velocity of small particles. Powder Technol. 125 (2–3), 131–139.

Ferry, J., Rani, S., Balachandar, S., 2003. A locally implicit improvement of the equilibrium Eulerian method. Int. J. Multiphase Flows 29, 869–891.

Foss, D., Brady, J., 2000. Structure, diffusion and rheology of Brownian suspensions by Stokesian dynamics simulations. J. Fluid Mech. 407, 167–200.

Fukushima, Y., Parker, G., Pantin, H., 1985. Prediction of ignitive turbidity currents in scripps submarine canyon. Marine Geol. 67, 55–81.

García, M., 1992. Turbidity currents. Encyclopedia of Earth System Science. Academic Press Inc., pp. 399–408.

García, M., 1994. Depositional turbidity currents laden with poorly sorted sediment. J. Hydra. Eng. 120 (11), 1240–1263.

García, M., Parker, G., 1989. Experiments on hydraulic jumps in turbidity currents near a canyon-fan transition. Science 245, 393–396.

García, M., Parker, G., 1993. Experiments on the entrainment of sediment into suspension by a dense bottom current. J. Geophys. Res. 98 (C3), 4793–4807.

Gladstone, C., Phillips, J., Sparks, S., 1998. Experiments on bidisperse, constant-volume gravity currents: propagation and sediment deposition. Sedimentology 45, 833–843.

Härtel, C., Meiburg, E., Necker, F., 2000. Analysis and direct numerical simulation of the flow at a gravity-current head. Part 1. Flow topology and front speed for slip and no-slip boundaries. J. Fluid Mech. 418, 189–212.

Heezen, B., Ewing, M., 1952. Turbidity currents, submarine slumps and the 1929 grans banks earthquake. Am. J. Sci. 250, 849–873.

Hopfinger, E., 1983. Snow avalanche motion and related phenomena. Ann. Rev. Fluid Mech. 15, 47–76.

Hoult, D., 1972. Oil spreading in the sea. Ann. Rev. Fluid Mech. 4, 341–368.

Huppert, H., 1982. The propagation of two-dimensional and axisymmetric viscous gravity currents over a rigid horizontal surface. J. Fluid Mech. 121, 43–58.

Huppert, H., Simpson, J., 1980. The slumping of gravity currents. J. Fluid Mech. 99, 785–799.

Joseph, D., Lundgren, T., 1990. Ensemble averaged and mixture theory equations for incompressible fluid-particle suspensions. Int. J. Multiphase Flows 16, 35–42.

Karamanos, G., Karniadakis, G., 2000. A spectral vanishing viscosity method for large-eddy simulations. J. Comp. Phys. 163, 22–50.

Kuenen, P., Migliorini, C., 1950. Turbidity currents as a cause of graded bedding. J. Geol. 58 (2), 91–127.

Machioro, M., Tanksley, M., Prosperetti, A., 1999. Mixture pressure and stress in disperse two-phase flow. Int. J. Multiphase Flows 25, 1395–1429.

Marble, F.E., 1970. Dynamics of dusty gases. Ann. Rev. Fluid Mech., 397–446.

Mohrig, D., Whipple, K., Hondzo, M., Ellis, C., Parker, G., 1998. Hydroplaning of subaqueous debris flows. Geol. Soc. Am. Bull. 110 (3), 387–394.

Necker, F., Härtel, C., Kleiser, L., Meiburg, E., 2002. High-resolution simulations of particle-driven gravity currents. Int. J. Multiphase Flow 28, 279–300.

Necker, F., Härtel, C., Kleiser, L., Meiburg, E., 2005. Mixing and dissipation in particle-driven gravity currents. J. Fluid Mech. 545, 339–372.

Normark, W., Dickson, F., 1976. Man-made turbidity currents in lake superior. Sedimentology 23, 815–831.

Parker, G., Fukushima, Y., Pantin, H., 1986. Self-accelerating turbidity currents. J. Fluid Mech. 171, 145–181.

Pope, S., 2000. Turbulent flows. Cambridge University Press, Cambridge, UK.

Prosperetti, A., 2001. Ensemble averaging techniques for disperse flows. In: Drew, D., Joseph, D., Passman, S. (Eds.), Particulate Flows Processing and Rheology, Springer, New York.

Rani, S., Balachandar, S., 2003. Evaluation of the equilibrium Eulerian approach for the evolution of particle concentration in isotropic turbulence. Int. J. Multiphase Flows 29, 1793–1816.

Shotorban, B., Balachandar, S., 2006. Particle concentration in homogeneous shear turbulence simulated via Lagrangian and equilibrium Eulerian approaches. Phys. Fluids 18 (6).

Simpson, J., 1997. Gravity Currents, second ed. Cambridge University Press.

Sparks, R., Carey, S., Sigurdsson, H., 1991. Sedimentation from gravity currents generated by turbulent plumes. Sedimentology 38, 839–856.

Squires, K., Eaton, J., 1991. Preferential concentration of particles by turbulence. Physics of Fluids A 3.

Tadmor, E., 1989. Convergence of spectral methods for nonlinear conservation laws. SIAM J. Num. Anal. 26, 30–44.

Wang, L., Maxey, M., 1993. Settling velocity and concentration distribution of heavy particles in isotropic turbulence. J. Fluid Mech. 256, 27–68.

Zhang, D., Prosperetti, A., 1997. Momentum and energy equations for disperse two-phase flows and their closure for dilute suspensions. Int. J. Multiphase Flows 23, 425–453.

Zhou, J., Adrian, R., Balachandar, S., Kendall, T., 1999. Mechanics for generating coherent packets of hairpin vortices. J. Fluid Mech. 387, 353–396.